Soft Matter



PAPER View Article Online
View Journal | View Issue



Cite this: *Soft Matter*, 2024, **20**, 1447

Received 3rd October 2023, Accepted 10th January 2024

DOI: 10.1039/d3sm01323e

rsc.li/soft-matter-journal

Sliding friction of a pillar array interface: part I†

Jasreen Kaur,^a Xuemei Xiao,^b Constantine Khripin,^c Chung-Yuen Hui * and Anand Jagota * * * * and Anand Jagota * * * * and * an

Biology is replete with examples, at length scales ranging from the molecular (ligand-receptor binding) to the mesoscopic scale (wing arresting structures on dragonflies) where shape-complementary surfaces are used to control interfacial mechanical properties such as adhesion, friction, and contact compliance. Related bio-inspired and biomimetic structures have been used to achieve unique interfacial properties such as friction and adhesion enhancement, directional and switchable properties. The ability to tune friction by altering surface structures offers advantages in various fields, such as soft robotics and tire manufacturing. Here, we present a study of friction between polydimethylsiloxane (PDMS) samples with surfaces patterned with pillar-arrays. When brought in contact with each other the two samples spontaneously produce a Moiré pattern that can also be represented as an array of interfacial dislocations that depends on interfacial misorientation and lattice spacing. Misorientation alone produces an array of screw dislocations, while lattice mismatch alone produces an array of edge dislocations. Relative sliding motion is accompanied by interfacial glide of these patterns. The frictional force resisting dislocation glide arises from periodic single pillar-pillar contact and sliding. We study the behavior of pillar-pillar contact with larger (millimeter scale) pillar samples. Inter-pillar interaction measurements are combined with a geometric model for relative sliding to calculate frictional stress that is in good agreement with experiments.

1. Introduction

Achieving tunable adhesion and friction has applications ranging from rubber processing in tire manufacturing to object handling in soft robotics. Nature has provided us with many examples of how microstructures on the surface can help control adhesion and friction. One such example is that of a gecko, Nhich has fibrillar structures on its toes to help it climb rough and smooth surfaces. Sp,10 Geckos stick using van der Waals dispersion forces and have reversible adhesion. Another such example is that of the head arresting system in dragonflies, which consists of intricate complementary microstructures on their head and neck to immobilize the head during tandem flight. Pillars in insects and amphibians

Bioinspired and biomimetic structures have been shown to modulate adhesion, $^{20-22}$ friction, 23 and contact compliance $^{6,24-28}$ and to provide new functionality such as switchability and directional properties just by altering surface structures. An exemplary instance is the renowned case of Velcro, 29 which operates on a loop-clasp mechanism. There is now a considerable literature on bioinspired contact surfaces. $^{3,9,14,15,20,30-38}$

Most bioinspired studies focus on adhesion/friction enhancement for microstructures on one side against a generic smooth or rough surface on the other. Shape complementary microstructures on both sides for the interface have been relatively less explored. It has been demonstrated that shape complementarity at the micron scale can significantly enhance adhesion selectivity. Guduru selectivity enhance adhesion selectivity. Guduru selectivity enhance and a rigid solid, uncovering an intriguing phenomenon. Surface waviness induces an unstable detachment process with alternating stable and unstable segments, resulting in increased work of separation. These findings provide an alternative explanation for the sometimes observed increase in pull-off force on rough surfaces. Adhesion selectivity using rippled surfaces showed

have liquid secretion^{14,15} to form a capillary bridge for adhesion. Many other animals like skinks,¹⁶ insects like beetles and spiders^{17–19} have microstructures on their contacting surfaces to achieve desired adhesion and friction.

^a Department of Chemical & Biomolecular Engineering, Lehigh University, Bethlehem, PA 18015, USA

b Department of Mechanical and Aerospace Engineering, Cornell University, Ithaca, NY 14853, USA. E-mail: ch45@cornell.edu

^c Michelin Americas Research Center, Michelin North America Inc., Greenville, SC, 29605, USA

^d Department of Bioengineering, Lehigh University, Bethlehem, PA 18015, USA. E-mail: anj6@lehigh.edu

^e Global Station for Soft Matter, GI-CoRE, Hokkaido University, Sapporo, Japan

[†] Electronic supplementary information (ESI) available. See DOI: https://doi.org/10.1039/d3sm01323e

Paper Soft Matter

how shape complementary surfaces can enhance adhesion. Singh et al. used microchannel structures⁴³ to show adhesion enhancement in such shape complementary interfaces. Chen et al. 40 showed the same using a pillar geometry.

The investigation of sliding friction in shape-complementary surfaces has been relatively limited. Amonton's and Coulomb's laws describe friction in phenomenological terms, but the understanding of the relationship between macroscopic frictional response and the behavior of microscopic contacts remains under active investigation. 48-50 He et al. 42 studied sliding friction in ridge-channel and pillar interfaces, achieving friction enhancement in structured surfaces as compared to control surfaces. They reported the spontaneous formation of interfacial dislocations and presented a model for friction in ridge-channel surfaces based on treating the dislocation core as a crack. However, they presented only a qualitative description of friction in pillar surfaces.

For periodically structured two-sided interfaces, orientational or lattice-parameter mismatch leads to spontaneous production of Moiré patterns on the interface, much like an incommensurate twist grain boundary in crystalline solids. These can also be represented as dislocation structures in shape complementary surfaces that resemble microscale replicas of dislocations on the atomic scale in crystalline solids. Therefore, models for dislocation glide and microscopic friction mechanisms are relevant. For instance, the Peierls/ Nabarro model for the dislocation core provides expressions for the minimum stress needed for dislocation glide. 51,52 The Prandtl-Tomlinson model⁵³ for nanoscale friction is a minimalistic model for the relationship between the energy of interaction between two surfaces and friction. 50,54 Related ideas have been used to explain friction in soft materials.^{55–57} The Frenkel-Kontorova (FK) model is similarly based on motion of a chain of particles placed on a periodic substrate and is used to describe sliding in crystalline interfaces. This model can be used to understand a pillar interface, where each pillar has to slide past pillars on the other side of the interface. 50,58

In this work we study friction in bioinspired, two-sided, micropillar surfaces. Our goal is to relate macroscopically measured friction stress, in terms of the pillar deformation at the interface. This problem is analogous to that of determining the stress needed for a dislocation to glide in a crystal, the basic version of which is determined by the Peierls-Nabarro model of the dislocation. 51,52,54,58-60 Analogously, for our model, friction is defined as the force required for Moiré patterns/dislocations to slide across the interface, the details of which depend on pillar-pillar interaction.

Experimental methods

2.1 Sample fabrication

Micropillar samples were fabricated using polydimethylsiloxane (PDMS) elastomer molded into an etched silicon master with pillar geometry on the surface patterned by photolithography. The pillars fabricated were 10 µm in diameter, 16 µm in height, and

arranged in a square array with a minimum interpillar spacing of 20 μm. PDMS precursor (silicone elastomer base) was combined with crosslinker (curing agent, Sylgard 184 Silicone Elastomer kit, Dow Corning) in the ratio 10:1 by weight. The mixture was then degassed under vacuum for 30 minutes before applying to the master and was cured at room temperature for 2 days. The cured PDMS was then peeled off the silicon master. A typical sample is 30 mm long, 10 mm wide and about 800 um thick. The second complementary sample was fabricated in a similar way. Additional samples were fabricated in a similar way but cured at different temperatures to introduce slightly different interpillar spacing due to differences in thermal contraction from curing to room temperature. Flat samples were also fabricated with no micropatterns and used for control experiments. A white light interferometry-based optical profilometer (Zegage, Zygo Corp) was used to produce micrographs of micropillar samples as shown in Fig. 1(a) and (b). Fig. 1(c) and (d) show a plan view of the interface each patterned with micropillars showing a misorientation, θ (Fig. 1c) or a lattice mismatch, λ (Fig. 1d) between the two arrays. The circles represent the bottom of the pillars where they join the bulk. Fig. 1c shows two pillar arrays (black and red lattices), in which the black lattice is rotated by a misorientation angle, $\theta = 10^{\circ}$, with respect to the red lattice. Fig. 1d shows two

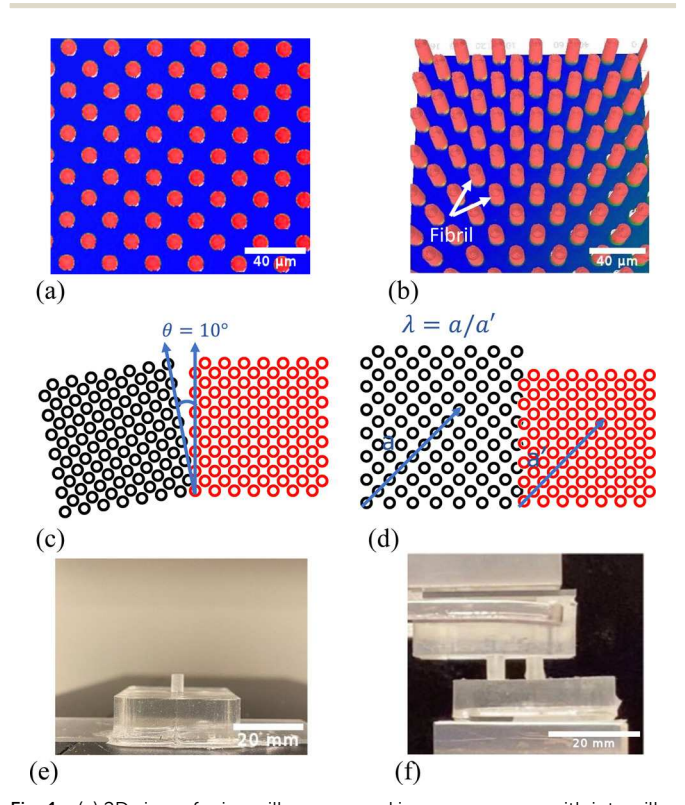


Fig. 1 (a) 2D view of micropillars arranged in a square array with interpillar spacing of 20 μ m. The pillars are 10 μ m in diameter and \sim 16 μ m in length. (b) 3D view of micropillars. (c) Arrays of black and red pillars at a relative misorientation angle, θ = 10°. (d) Red and black pillar arrays with lattice spacing mismatch, $\lambda = (a/a') = 1.2$. (e) Picture of a mm-scale, single pillar sample. (f) Image of two mm-scale single pillar samples, mounted on a custom built tribometer

lattices with different minimum spacings a and a' where $\lambda = a/a'$ is the lattice mismatch. (In the case shown here, $\lambda = 1.2$).

Soft Matter

In order to study inter-pillar interaction, larger, mm-scale, single pillar samples were fabricated, as shown in Fig. 1(e), with the same aspect ratio as the micropillars. The process included using the same PDMS mixture and pouring the mixture into a mold fabricated for this purpose. The cured single pillar samples were 3 mm in diameter and 4.8 mm in height with backing dimensions of 30 mm \times 30 mm \times 8 mm shown in Fig. 1e and f. Details of the single pillar experiments and its analysis are given in the companion paper.61

2.2 Friction measurement

Friction measurements were conducted using a custom built Flat-on-Flat Tribometer as shown in Fig. 2a. The setup consists of two stages on which samples are mounted, and a load cell

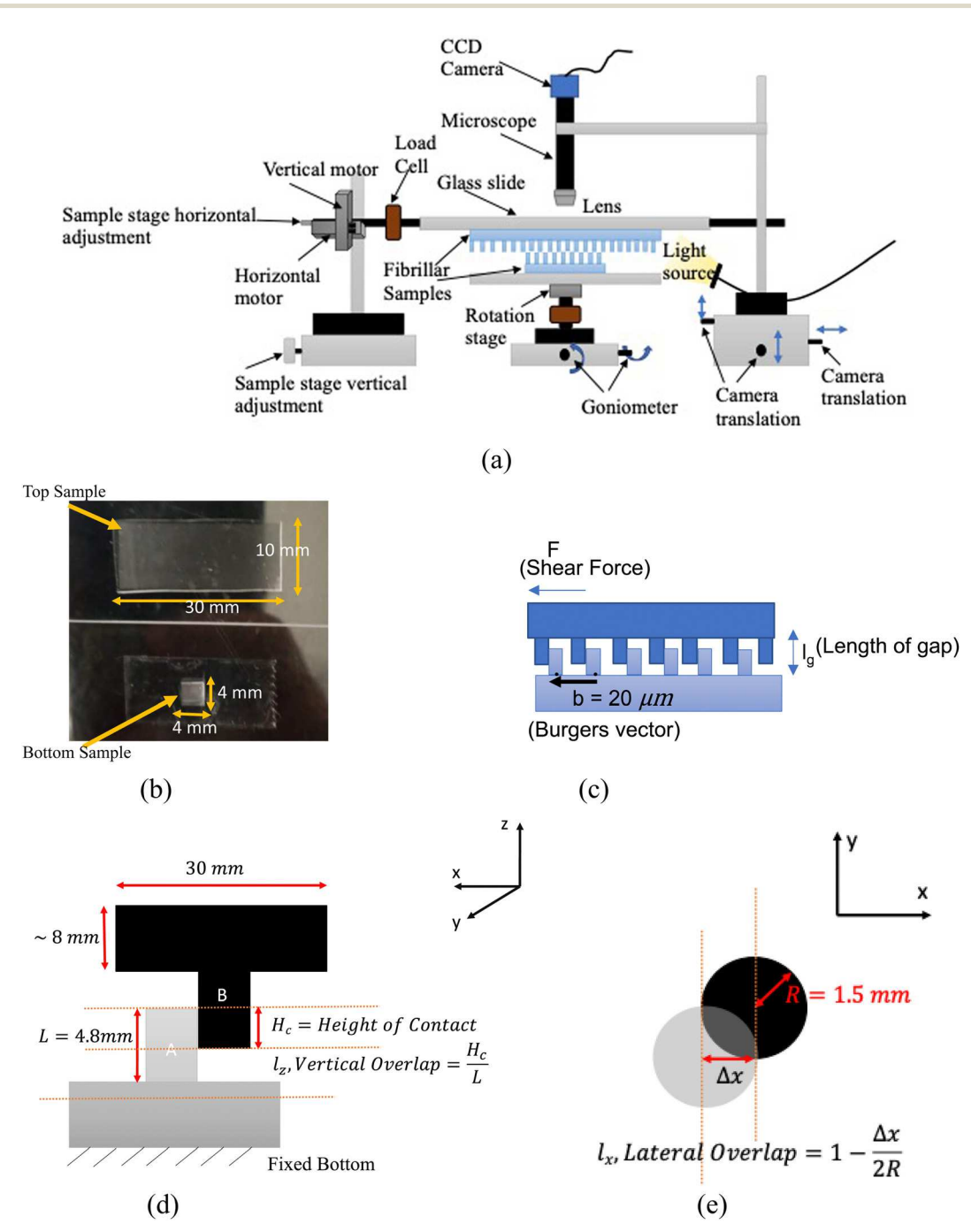


Fig. 2 (a) Schematic of custom-built flat-on-flat tribometer. Pillar samples are mounted on upper and lower stages as shown. Vertical and horizontal motors control the relative displacement between two samples. (b) Micropillar PDMS samples for measuring sliding friction, Top sample has dimensions 30 mm by 10 mm and bottom sample is 4 mm by 4 mm. (c) Schematic of pillar samples in contact showing the Burgers vector for pillar samples. (d) Schematics of single pillar samples, H_C = height of contact or vertical overlap (e) l_x = lateral overlap.

each to measure horizontal or shear force, and vertical or normal force. Vertical and horizontal motors control the respective movement of stages, and the rotation motor controls rotation of the lower stage (to control misorientation). The motors are connected to a motion controller and the entire system is controlled by custom-written LabVIEW code. A camera is used to image the behavior of pillars at the interface during

Sliding friction was measured at five different values of misorientation ($\theta = 0^{\circ}$, 5° , 15° , 30° , 45°) and five different normal loads (0.075 N to 0.4 N) for patterned and flat control samples and each experiment was repeated three times. The setup can work under normal load or displacement control. Normal load is controlled by normal displacement, which is fed to the PID controller operated by LabVIEW software. The two samples are brought in contact using the vertical motor.

A typical friction experiment consists of sticking the top and bottom samples to glass slides using double-sided Scotch® tape. The slides are mounted onto the lower and upper stages and brought into contact under displacement control (Fig. 2a). After mounting the samples on the stage, we set the misorientation angle between the two samples using the rotation motor. We start by aligning the two samples at 0° misorientation, which is when dislocations disappear from the interface. With this as $\theta = 0^{\circ}$, other angles are easily obtained. Once we have the desired misorientation, we set a normal load and switch to normal load control. When the load stabilizes to the set value, we slide the samples with respect to each other for 3 mm at a velocity of 0.01 mm s^{-1} .

3. Results and discussion

3.1 Moiré patterns & dislocations

When the two micropillar samples are first brought in contact, Moiré patterns appear spontaneously on the interface, as we've reported previously.41-43 Due to the square patterning and periodicity, the interface consists of periodic square regions, and the size of these regions depends on the misorientation and lattice spacing mismatch. 42,62 The boundary of each square region can be viewed as a dislocation line, albeit with a diffuse core. Specifically, these regions are formed by two parallel sets of mutually perpendicular dislocation lines (see Fig. 3). We refer to the edges in the Moiré patterns as "dislocation lines" by analogy to twist grain boundaries in crystals. 62,63 Although they are geometrically similar to twist grain boundaries, the mechanics of interaction across the interface is different as discussed later.

The Moiré pattern and its accompanying dislocation array forms during the initial application of normal load, with density and orientation depending on λ and θ values. Orientational mismatch alone, ($\theta > 0^{\circ}$ at $\lambda = 1$), produces an array of screw dislocations whereas a lattice mismatch alone, ($\lambda \neq 1$ at $\theta = 0^{\circ}$), produces an array of edge dislocations. Presence of both, an orientation mismatch and a lattice mismatch, produces an array of mixed dislocations.⁴² The density of square regions

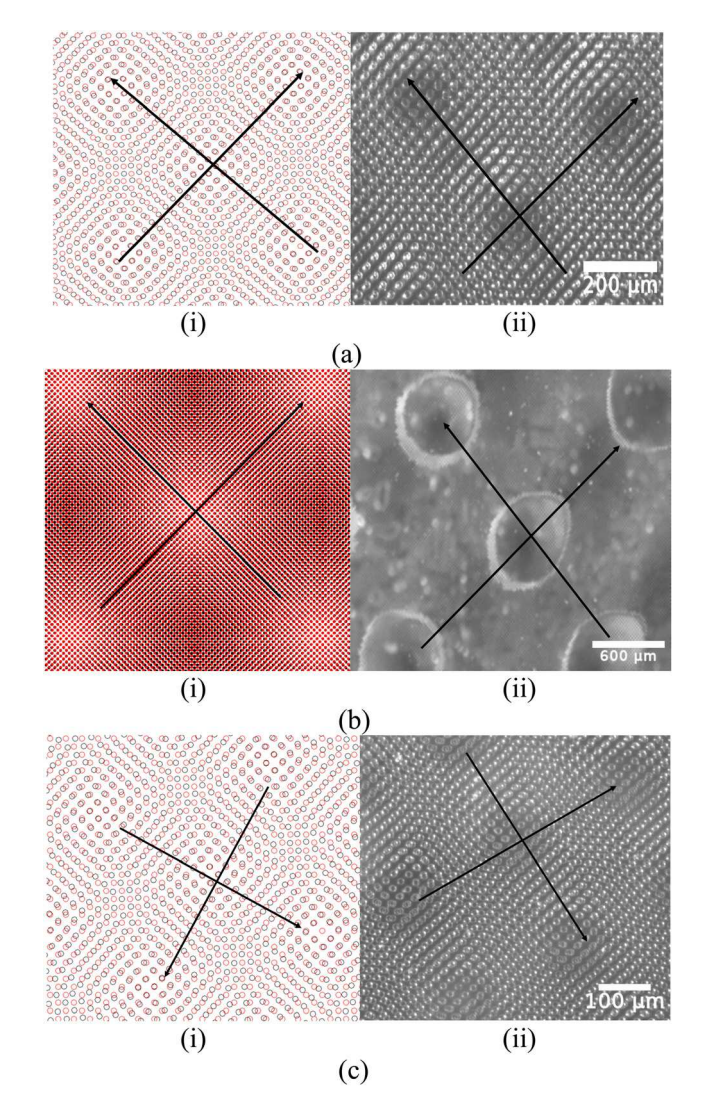


Fig. 3 Moiré pattern & Dislocation lines. Representation of Moiré patterns as screw, edge, and mixed dislocations. (3a)(i) An array of screw dislocations produced by aligning red and black lattices at a misorientation, $\theta = 5^{\circ}$ and $\lambda(a/a') = 1$. (3a)(ii) An array of screw dislocations formed at the interface of two pillar samples in contact. (3b)(i) An array of edge dislocations produced when two lattices (here, red and black) have a lattice mismatch, $\lambda(a/a') = 1.023$. (3b)(ii) An array of edge dislocations formed at the interface of two pillar samples in contact at $\lambda(a/a') = 1.023$. Note difference in scale between 3a(ii) and 3b(ii). (3c) (i) an array of mixed dislocations produced by aligning the two lattices at a misorientation θ = 5° and at lattice mismatch, $\lambda(a/a') = 1.023$. (3c)(ii) An array of mixed dislocations on the pillar interface with the same conditions as 3c(i).

increases with increase in mismatch.⁴² Fig. 3 shows formation of Moiré patterns⁶⁴ between shape complementary pillar samples. Fig. 3a(i) represents geometrically the formation of screw dislocations when red and black square lattices overlap at a 5° misorientation. As noted above, the black arrow lines in Fig. 3 represent dislocation lines. A corresponding pattern can also be clearly seen on the interface of our actual pillar samples in Fig. 3a(ii) for the same misorientation angle. As sliding begins, pillars are pushed into contact, each with a neighboring pillar with force that changes with displacement until it loses contact

with its partner pillar. This process occurs for each pillar. In the micrographs of Fig. 3, we observe a pattern of light and dark regions. The lighter patterns correspond to when pillars from complementary surfaces are in partial or full registry (i.e., right next to each other). The darker regions are where pillars from both samples are bent on top of each other and are at maximum disregistry. The lines connecting dark regions can be interpreted to be dislocation lines.

Fig. 3b compares the formation of Moiré patterns corresponding to edge dislocations geometrically and in experiments. Fig. 3b(i) shows that red and black lattices with $\lambda = 1.023$ form edge dislocations. Similar patterns are observed experimentally as shown in Fig. 3b(ii). Edge dislocations appear on a perfectly aligned interface with lattice mismatch. As misorientation is then increased from $\theta = 0^{\circ}$, Moiré patterns corresponding to mixed dislocations appear on the interface (shown in Fig. 3c). Fig. 3b(ii) represents experimentally observed edge dislocations at $\lambda = 1.023 \pm 0.001$. The pattern again shows light and dark regions. Fig. 3c(i) represents Moiré patterns corresponding to dislocations with mixed edge and a screw character for λ = 1.023 and $\theta = 5^{\circ}$. The patterns are different than that of screw dislocations if observed carefully in that they are tilted slightly compared to the orientation of screw dislocations. Fig. 3c(ii) represents mixed dislocations for pillar samples in contact at λ = 1.023 \pm 0.001 and θ = 5°. A more detailed account of the geometry of dislocation arrays can be found in ref. 42. For

completeness, we provide the main results. These are that the dislocation density ρ and orientation α of the dislocation lines are functions of misorientation angle, θ , and lattice mismatch, λ . Orientation, α is found as,

$$\alpha = \tan^{-1} \frac{\sin \theta}{\lambda - \cos \theta},\tag{1}$$

and

density as
$$\rho = \frac{1}{b} \sqrt{(\lambda - 1)^2 + 4\lambda \sin^2\left(\frac{\theta}{2}\right)}$$
 (2)

where b is the magnitude of the Burgers vector \boldsymbol{b} , λ is lattice mismatch, and θ is misorientation.

To further analyze the orientation of moving dislocations, it is useful to consider the Peach-Kohler force,⁵⁸ which is a configurational force that defines the direction of dislocation motion. It is given by

$$F_{\rm PK} = (\boldsymbol{\sigma} \cdot \boldsymbol{b}) \times \boldsymbol{\xi},\tag{3}$$

where σ is applied stress, and ξ is the dislocation line vector (see Fig. 4a and b for frame of reference). For a screw dislocation as shown in Fig. S17d (ESI \dagger), Burgers vector, b_1 is associated with the dislocation line AA'' and b_2 is associated with dislocation line CC". Thus, for a screw dislocation, there are

two Burgers vectors *i.e.*, $\boldsymbol{b}_1 = -\frac{1}{\sqrt{2}}\boldsymbol{e}_1 + \frac{1}{\sqrt{2}}\boldsymbol{e}_2$ and $\boldsymbol{b}_2 = \frac{1}{\sqrt{2}}\boldsymbol{e}_1 + \frac{1}{\sqrt{2}}\boldsymbol{e}_2$

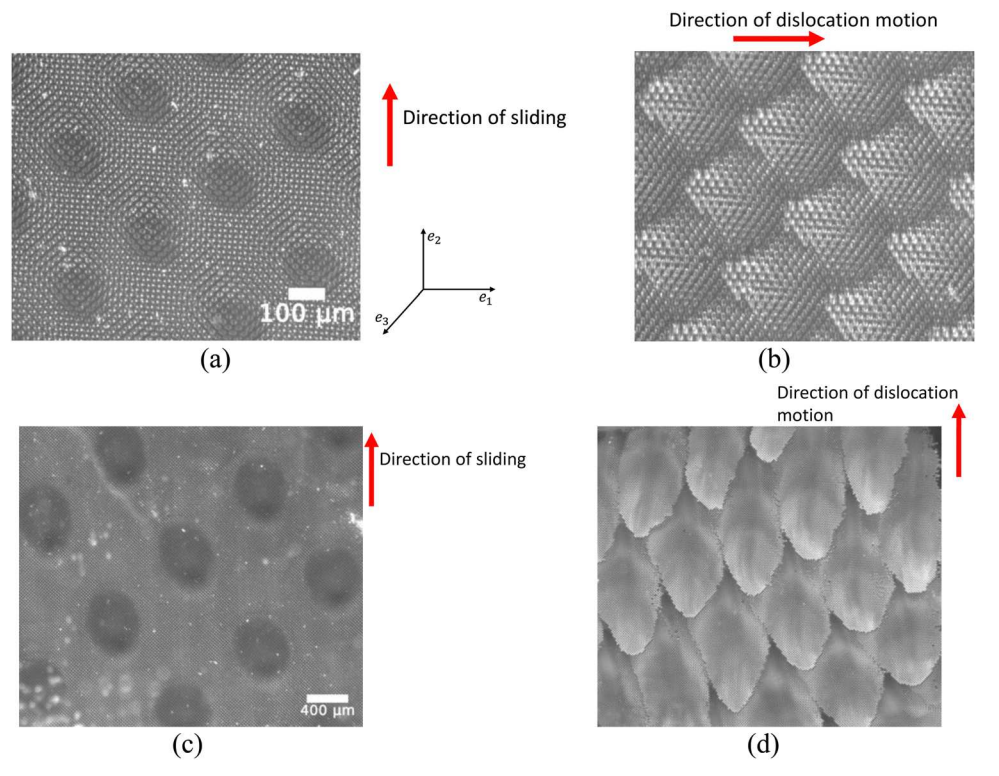


Fig. 4 Sliding happens through dislocation glide. Optical images of pillar interface. (a) Screw dislocations: at misorientation, $\theta = 5^{\circ}$, $\lambda = 1$ (before sliding commences), (b) snapshot of sliding screw dislocations at misorientation, $\theta = 5^{\circ}$, $\lambda = 1$. For sliding in '2' direction, the dislocation pattern moves in 1' direction. (c) Edge dislocations: at misorientation, $\theta = 0^{\circ}$, $\lambda = 1.023$ (before sliding commences), (d) snapshot of sliding edge dislocation pattern at $\lambda = 1.023$. For sliding in '2' direction, the dislocation pattern moves in '2' direction.

Paper Soft Matter

 $\frac{1}{\sqrt{2}}e_2$, ξ is the dislocation line vector, $\xi_1 = -\frac{1}{\sqrt{2}}\overline{e_1} + \frac{1}{\sqrt{2}}\overline{e_2}$, and $\xi_2 = \frac{1}{\sqrt{2}} \overline{e_1} + \frac{1}{\sqrt{2}} \overline{e_2}$ and stress, $\sigma = -\tau e_2 \otimes e_3 - \tau e_3 \otimes e_2 + \frac{1}{\sqrt{2}} \overline{e_1} \otimes e_2$ $pe_3 \otimes e_3$, thus, $F_{PK} = \tau \left(\frac{1}{2} \overline{e_1} + \frac{1}{2} \overline{e_2} \right)$ and $F_{PK} = \tau \left(\frac{1}{2} \overline{e_1} - \frac{1}{2} \overline{e_2} \right)$. This gives the resultant force in $\overline{e_1}$ direction and this implies that screw dislocation runs perpendicular to the direction of sliding which is true as shown in Fig. 4b (full video in ESI,† SI: V3_lambda=1_5_deg_ ScrewDislocation.avi). For an edge dislocation as shown in Fig. S17e (ESI†), Burgers vector b_1 is associated with dislocation line C'C" and Burgers vector b_2 is associated with dislocation line A'A". Thus, $b_1 =$ $\frac{1}{\sqrt{2}}e_1 - \frac{1}{\sqrt{2}}e_2$, $b_2 = \frac{1}{\sqrt{2}}e_1 + \frac{1}{\sqrt{2}}e_2$, and corresponding dislocation line vector, $\xi_1 = \frac{1}{\sqrt{2}} e_1 + \frac{1}{\sqrt{2}} e_2$, $\xi_2 = -\frac{1}{\sqrt{2}} e_1 + \frac{1}{\sqrt{2}} e_2$, $F_{\mathrm{PK}} = \tau \left(-\frac{1}{2} \, \overline{e_1} + \frac{1}{2} \, \overline{e_2} \right)$ and $F_{\mathrm{PK}} = \tau \left(\frac{1}{2} \, \overline{e_1} + \frac{1}{2} \, \overline{e_2} \right)$ respectively. Net resultant force, F_{PK} is in $\overline{e_2}$ direction, which implies that for an edge dislocation, dislocation lines run

parallel to the direction of sliding as shown in Fig. 4c and d

and a full video in ESI† (SI: V8 lambda=1.023 0deg EdgeDislocation).

Fig. S17 (ESI†) and Fig. 4 show that, as we traverse the sample, the registry between pillars above and below the interface varies systematically and periodically, with period identical to that of the Moiré pattern. We see that the direction of dislocation motion is consistent with that given by the Peach-Kohler formula. When sliding initiates, the interface loses its symmetry (compare Fig. 4a-d). The period of the Moiré pattern corresponds to disregistry equal to the Burgers vector. Therefore, for one Burgers vector of slip in the '2' direction, each pillar undergoes a full loadrelease cycle. This observation is key for our calculation of macroscopic friction stress. That is, at any point in time, the instantaneous friction force is the sum of all pairwise inter-pillar contact forces across the interface. The friction force averaged over one sliding cycle (slip = Burgers vector) can be obtained by matching external work done to the energy loss for each pillar pair in going through a full loading-unloading cycle.

3.2 Friction stress measurements

Fig. 5(a) shows typical raw data for measured friction stress as a function of sliding distance, for different values of normal stress varying from 4 \times 10³ N m⁻² to 2.5 \times 10⁴ N m⁻² at

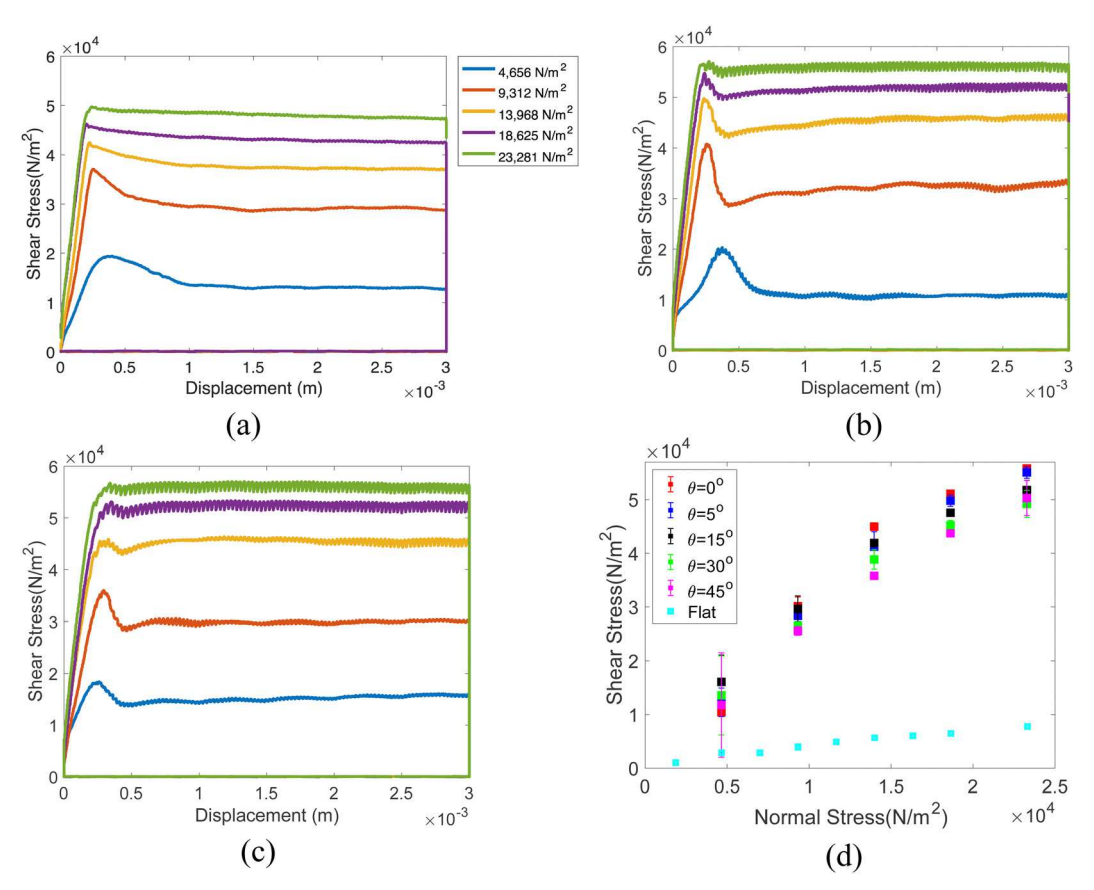


Fig. 5 Experimental data for friction. (a) Friction stress as a function of displacement for no lattice mismatch i.e., $\lambda = 1$, but $\theta = 5^{\circ}$ at various normal loads. (b) Friction stress as a function of displacement at a lattice mismatch $\lambda = 1.023$ for misorientation $\theta = 0^{\circ}$. (c) Friction stress as a function of displacement at a lattice mismatch i.e., $\lambda = 1.023$ for misorientation $\theta = 5^{\circ}$. (d) Steady state friction stress as a function of normal stress at a lattice mismatch $\lambda = 1.023$ for several misorientations from θ = 0° to θ = 45° and normal load, in comparison with a flat control sample

 $\lambda = 1$ and $\theta = 5^{\circ}$ (dislocations have screw character). As the pillar samples come in contact and start sliding, friction force first rises and then subsides to an approximately constant value. Note that the friction stress increases with increasing normal stress. (Friction stress is obtained by averaging friction force when it stabilizes between 2 to 3 mm of shear displacement and then dividing it by the nominal area of contact, which in this case is sample size i.e., $4 \times 4 \text{ mm}^2$.) Fig. 5b shows how the friction stress varies with displacement for edge dislocation case at $\lambda = 1.023$ and $\theta = 0^{\circ}$. Fig. 5c shows data for friction stress *versus* displacement for mixed dislocation case at $\lambda = 1.023$ and $\theta = 5^{\circ}$. The data show that friction stress is strongly dependent on pressure and does not depend much on edge or screw character of dislocation nor on misorientation if λ is close to unity.

Fig. 5d shows a plot of how friction stress varies as a function of normal load and misorientation, θ . This particular case is at $\lambda = 1.023$ for various values of $\theta = 0^{\circ}$, 5° , 15° , 30° and 45°. As can be seen from the Fig. 5d, friction rises strongly with the normal stress but is essentially independent of misorientation. This is starkly different from that found in the ridgechannel geometry⁴³ where friction depends strongly on misorientation angle. Weak dependence on misorientation for pillar samples is likely because pillars are organized in a square lattice, which is not far from isotropic. Also shown in Fig. 5(d) is measured friction stress for a control in which one of the pillar interfaces is replaced by a flat, unstructured, PDMS sample. Friction for cases where both sides have pillars shows significant increase as compared to friction in the control case. Friction stress for pillar complementary samples can be seen to be enhanced by up to about a factor of 5 over that of a control sample.

We turn our attention next to studying the relationship between macroscopically observed friction and the pairwise interaction of pillars. For this purpose, we first show results on single pillar-pair experiments and then combine these with a geometric model of the sliding interface to calculate predicted macroscopic friction stress.

3.3 Single pillar pair friction experiments

We propose that the friction force arises from the ensemble of pillar-pillar interactions. To study this quantitatively and directly, we first conduct experiments on the interaction of pairs of pillars. Single pillar samples are fabricated following the process mentioned in Section 2.1. Pairs of these singlepillar samples are slid past each other. The contact is characterized by two types of overlaps between pillars: in the plane of the interface (lateral overlap) and along the length of the undeformed pillar (vertical overlap or H_c as height of contact) as shown in Fig. 2d, e and 6a, b.

The experiments are performed keeping the vertical distance between two pillars fixed. Let the length of each pillar be L. If the gap exceeds the upper limit (2L), we have zero vertical overlap. Then the pillars disengage and the force they transmit to each other while sliding goes to zero. If the gap hits the lower limit (L), then the pillar can take any vertical load.

Fig. 6a represents a lateral overlap that varies from 0 to 1, where l_x is a dimensionless parameter to measure lateral overlap and is defined as, $l_x = 1 - \frac{\Delta x}{2R}$. Fig. 6b represents vertical overlap along the length of the pillar and is defined as $l_z = \frac{H_c}{I}$ Fig. 6c-h shows a schematic progression of sliding a pair of pillars past each other. The collection of forces resisting this motion gives rise to the macroscopic friction force as well as the vertical reaction force.

Neglecting the role of adhesion (see experiments in ESI,† Section S3 on lubricated vs. dry single pillar pair experiments), we make the approximation that if we normalize all displacements and location by pillar radius and stresses by the shear modulus, then the normalized stress is a function of normalized location. That is, if one scales the system uniformly, forces measured in the pillar-pair interaction experiments can simply be scaled down to estimate forces in the micropillar samples. A series of figures in Fig. 6c-h shows progression of sliding for a typical single pillar-pair experiment. The corresponding shear and normal force plots are shown in Fig. 7 as a function of shear displacement. As the sliding starts under normal displacement control (i.e., vertical overlap is fixed for each experiment and normal load varies), the two pillars come in contact and bend as shear displacement increases. The two pillars appear to stick to each other as shear stress/force reaches a maximum point and then series of slipping events occur, accompanied by decrease of shear force, and ending with separation of the two pillars. (The case shown here in Fig. 6c-h is for a 100% lateral overlap, $l_x = 1$).

Fig. 7a shows variation of shear force with sliding displacement for single pillar pair experiments for lateral overlap, $l_x = 1$ at different vertical overlaps ranging from (4.8 mm to 0.8 mm). Shear force is maximum for maximum lateral overlap $(l_x = 1)$ and H_c = 4.8 mm and decreases if the lateral overlap or height of contact is decreased (as shown in Section S3 in ESI†). After contact, the shear force initially increases linearly with shear displacement. At an intermediate shear displacement, the response softens and then hardens again prior to initiation of stick-slip. As seen from Fig. 7a, after shear displacement reaches ~ 8 mm, there is a decline in shear force as the pillars slide with respect to each other in stick-slip steps. This stick slip motion, as the force declines, is most significant in the 100% lateral overlap case, whereas the force drop in the rest of the cases $(l_x = 0.75, 0.5, 0.25, 0)$ is more sudden (shown in ESI†). Normal force, on the other hand, rises initially but declines as shear force slope increases. This is because the two pillars in contact are almost horizontal (more force in shear direction) and thus normal force declines.

Fig. 7a and b also show quartic fits to the experimental data. The detailed mechanics of this inter-pillar interaction is presented in a companion paper. 61

The single pillar pair experiments provide:

$$T(u_s), N(u_s), u^*$$

$$w = \int_0^{u^*} T(u_s) du_s$$
(4)

Paper Soft Matter

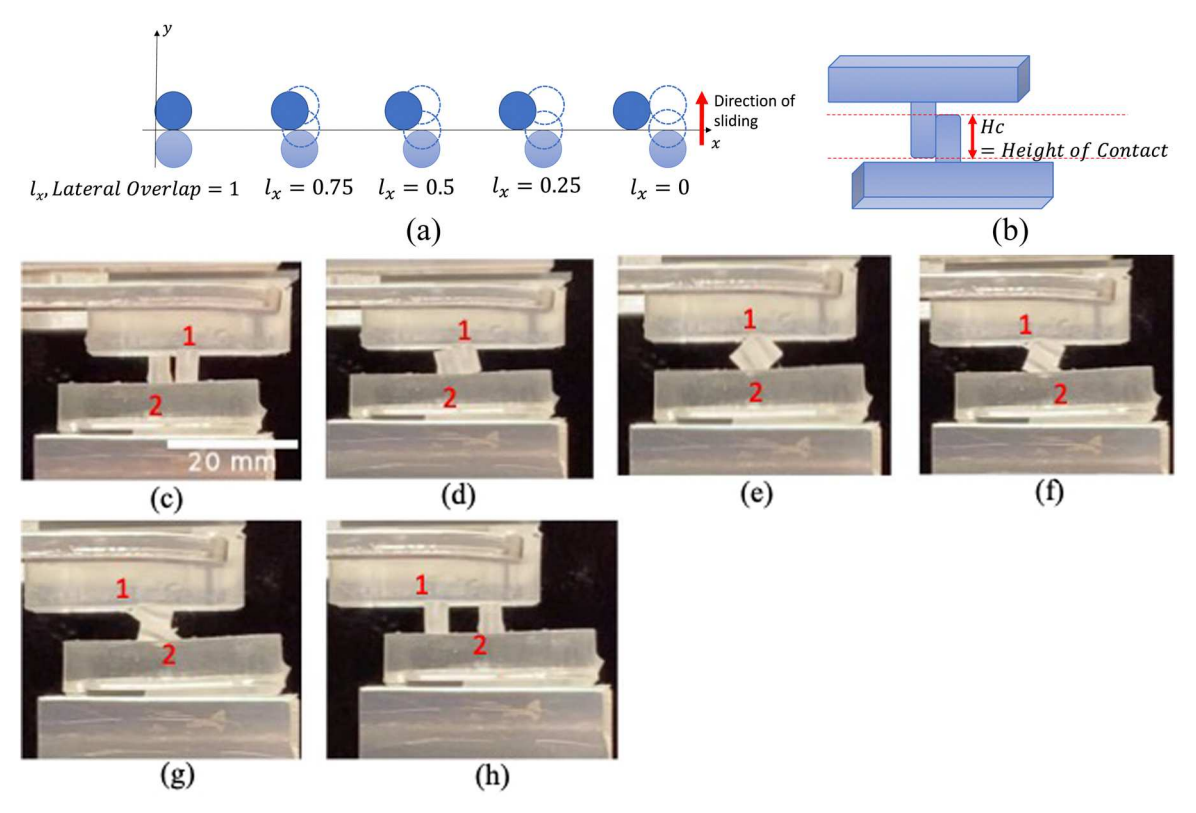


Fig. 6 Representation of different pillar overlaps and single pillar pair experiment. (a) Lateral overlaps, l_x ranging from 1 to 0. (b) Vertical overlap or height of contact (H_c) which ranges from 4.8 mm (full contact) to 0.8 mm (least contact). (c-h) Sliding experiment for a single pillar pair (1 & 2, side view). Progression of pillar contact during sliding at $l_x = 1$ and full height overlap ($H_c = 4.8$ mm).

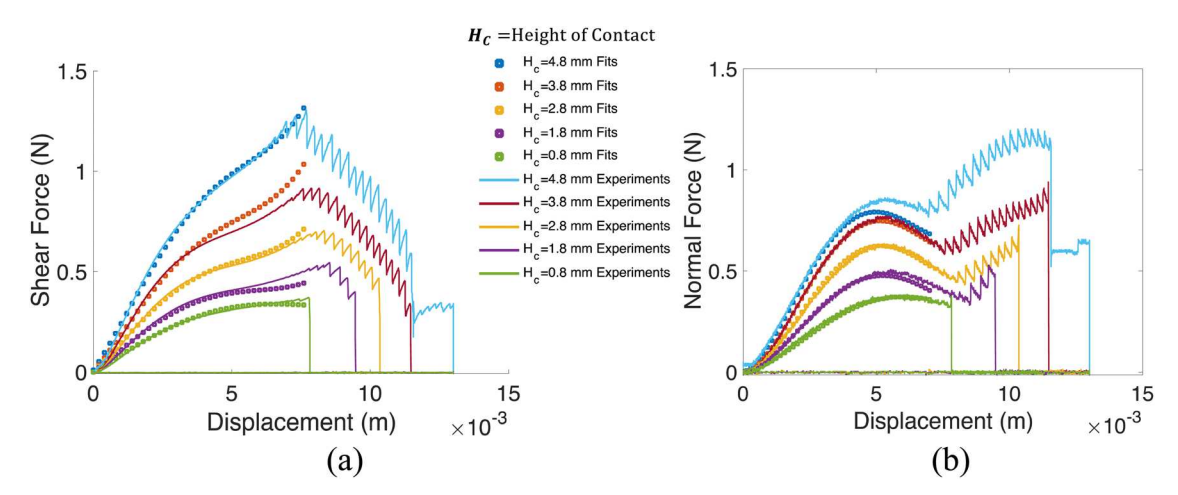


Fig. 7 Friction data for single pillar pair experiments. (a) Shear force as a function of shear displacement for 100% lateral overlap ($l_x = 1$) at different heights of contact, H_c (b) normal force as a function of shear displacement for 100% lateral overlap ($l_x = 1$) at different heights of contact, H_c (4.8 mm to 0.8 mm).

where, T, N, u^* , u_s , and w are shear force, normal force, maximum shear displacement, shear displacement, and energy loss from a single pillar pair, respectively. As shown in ESI,† the effect of adhesion is negligible so that change of scale leaves all stresses unchanged. Therefore, if the scale factor between the single pillar pair experiments and the pillar array is α_s , then energy scales as $(\alpha_s)^3$, displacement by α_s , and forces by $(\alpha_s)^2$.

Thus, for given overlap between a pair of micropillars, we may use the results of the mm-scale single pillar pair experiments to compute the shear and normal force of interaction for given lateral and vertical overlap of a pair of micro-pillars.

Each single-pillar-pair experiment is conducted for five specified values of lateral and vertical overlap ($5 \times 5 = 25$ cases in all) producing data such as shown in Fig. 7a and b (see also

ESI,† Fig. S7 and S8). Each force plot is fit with four fitting parameters. Each fitting parameter is a function of the two overlap parameters i.e., lateral overlap and vertical overlap or height of contact (H_c) . Thus, we have a 2D surface for each parameter (more information provided in ESI,† Fig. S15) that is fit by a third order polynomial in two variables (lateral and vertical overlaps) using which we can estimate the shear and normal forces for any specified overlaps.

3.4 Overall friction response

This section presents a geometric model illustrating the interaction between cylindrical pillars as they slide past one another. Fig. 8(a) shows two circles (representing pillars) sliding past each other with some lateral overlap, $l_x = \frac{|\Delta x|}{2R}$. Here, Δx denotes the lateral displacement between the centers of the two pillars, and R is the radius of each pillar. The upper pillar is shown in a sequence of positions (numbered 1 to 4) as it moves vertically by a distance 'dy' at each step. The deflection, δ , which quantifies the deviation of the pillars from their initial positions during sliding, is determined for each step. The deflection is expressed as:

$$\delta = \begin{cases} 2R - d, & 2R - d > 0 \\ 0, & 2R - d < 0 \end{cases}$$
 (5)

where d represents the distance between the centers of the two pillars and is calculated using the equation:

$$d = \sqrt{\Delta x^2 + \Delta y^2}; \ \Delta x = x_2 - x_1; \ \Delta y = y_2 - y_1$$
 (6)

thus, deflection simplifies to $\delta = 2R - \sqrt{\Delta x^2 + \Delta y^2}$, when 2R > d.

The final displacement in sliding direction, u_f , is derived from the initial displacement at which the pillars first come into contact, denoted as u_i , and is defined by:

$$u_{\rm f}$$
 (Final displacement) = $-(\Delta y - u_{\rm i})(0 \le u_{\rm f} \le 4R)$ (7)

This calculation also mirrors the physical bending of single pillars observed in sliding experiments. As the red lattice slides over the black lattice, the model calculates the displacement (in sliding direction) of each red pillar at every point in time, setting the displacement to zero once the distance between the centers of the pillars exceeds 2R. Initial displacement is defined as,

$$u_i = \sqrt{((2R)^2 - \Delta x^2)},$$
 (8)

which indicates the displacement at which pillars begin to overlap.

Fig. 8(b) visualizes the overall experimental setup with stationary lattice of large black pillars rotated by 5° with respect to z-axis, and a lattice of smaller red pillars sliding over the black lattice. The aim is to calculate shear stress that arises due to interaction between overlapping pillars. In the sliding lattice model, the calculation of shear and normal force begins with the determination of the final displacement, u_f of each red pillar, which is analogous to the physical displacement observed in single pillar sliding experiments (Fig. 7a and b). This final displacement is tracked until the inter-pillar distance exceeds twice the radius, effectively reducing the displacement to zero for calculation purposes.

The force-versus-displacement curves derived from single pillar experiments are processed through a quartic polynomial fitting procedure (with zero intercept). This yielded a set of four coefficients for each curve, and these coefficients are functions of two parameters: the lateral overlap, l_x and the height of contact, H_c . Through this functional relationship, we formulated a series of surface functions that map the dependency of these coefficients on the overlap parameters.

The simulation is carried out for fixed gap and this functional mapping allows us to interpolate between measured overlaps for predicting the system's response to varying degrees of overlap between the pillars. To provide a visual illustration of

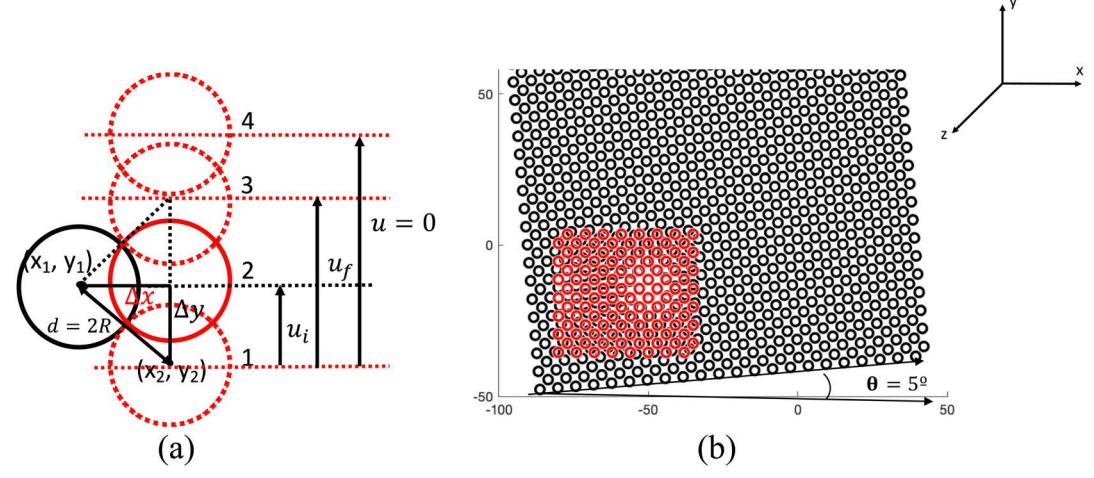


Fig. 8 Geometric model (a) geometry of two pillars sliding past each other with Δx lateral overlap. We imagine that the lower pillar is fixed while the upper one moves. (b) Geometric representation of overall experiment using large black lattice rotated by 5° w.r.t z axis and overlapping with a smaller red lattice sliding on the top.

Paper Soft Matter

these relationships, contour plots for each surface function have been included in Fig. S15a and b (ESI†).

With the surface functions defined, we are able to determine the coefficients for any specified combination of lateral and height overlaps. These coefficients, when applied in conjunction with the final displacement values, enable us to compute the shear and normal force. This approach allows for an accurate quantification of shear and normal forces. These individual forces from pairs of pillars are subsequently summed and divided by the sample area to ascertain the average shear and normal stress across the lattice.

The shear stress vs. normal stress predictions yielded by our model align closely with the empirical data from microscale friction experiments, remaining within the experimental shear stress range. Fig. 9(a)–(c) display the comparison of shear stress versus normal stress values obtained from the model with experimental data for various values of λ and θ .

Fig. 9a presents a comparative analysis of shear stress *versus* normal stress, specifically for a lattice parameter, λ , set to 1 across various angles of rotation, θ . The correlation between the model's predictions and the experimental data is generally favorable, however, an anomaly is observed for the case where $\theta=0^{\circ}$, the red curve. In this specific instance, the model predicts a sawtooth pattern in the shear force curve, diverging from the experimental trend. This deviation is attributed to the absence of edge-nucleated dislocations within the model's framework for the $\theta=0^{\circ}$ scenario. Consequently, the sawtooth pattern leads to a lower average shear stress in comparison to both the experimental data and the other curves represented for different θ values.

For a more detailed theoretical underpinning, including a comparison with a one-dimensional edge dislocation model, readers are directed to the ESI,† Section S4. This section discusses how the force summation approach used here aligns with energetic methods traditionally employed in the computation of average friction stress. See also Section S6 in ESI,† which contains a simple model that shows why summation of forces calculated using isolated pairs of pillars works because the pillars are highly compliant.

4. Summary and conclusions

We presented a study of friction of shape-complementary pillar interfaces. The structure of the interface can be understood to comprise Moiré patterns that accommodate misorientation and differences in lattice spacing on two sides of the interface. Relative sliding of such complementary pillar structures can be viewed as being accommodated by glide of Moiré patterns. The frictional force depends strongly on pressure but only weakly on misorientation. Friction for complementary pillar structures is higher than that of control samples by up to a factor of 5. In order to relate macroscopic measured friction to the behavior of single pillar-pair interactions, we conducted mm-scale single pillar-pair experiments and obtained pillar-pillar interaction forces at the interface. Using these data, we developed a simple numerical model to determine the sliding friction of the pillar interface as a sum of pairwise pillar-pillar interactions. Our model compares well with experiments.

This pillar interface has many similarities to atomistic interfaces. The interaction of atoms inside the dislocation core determines the force required to move a dislocation. In our case, the relevant interaction is that between pillars on opposite sides of the interface. An important difference between our interfacial structure and that found in crystalline interfaces at the atomic scale is that the summed mechanics of pillar pairs suffices to obtain the total friction stress. That is, pillar–pillar coupling is very stiff. In ESI,† S6 we present a simple model for an incommensurate pillar pair array which shows how, for sufficiently stiff pillars the system would behave more like atomistic interfaces do, with disregistry confined to dislocation lines.

Our results show how shape complementary pillar interfaces can be designed for enhanced, sliding friction.

Data availability

The data presented in this paper are available from the authors on reasonable request.

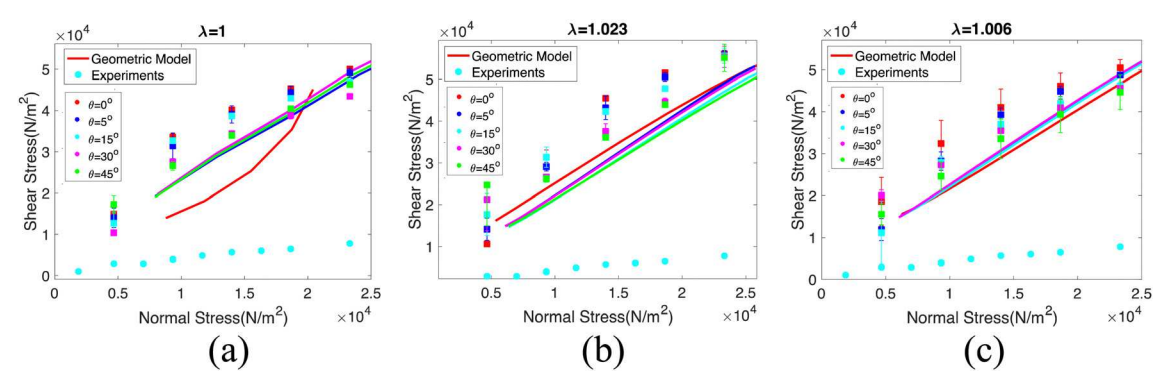


Fig. 9 Comparison of friction data from single pillar-pair experiments to that from geometric model simulations. Comparison of shear stress as a function of normal stress for geometric model and experiments at several misorientations $\theta = 0^{\circ}$, 5° , 10° , 15° , 30° , 45° at lattice mismatch, (a) $\lambda = 1$ (b) $\lambda = 1.023$ (c) $\lambda = 1.006$.

Conflicts of interest

The authors declare no conflict of interest.

Acknowledgements

We acknowledge support from the National Science Foundation through the Grant LEAP-HI: CMMI-1854572. We would also like to acknowledge useful discussion with Mike Andrews.

References

- 1 C. Menon, M. Murphy and M. Sitti, Gecko inspired surface climbing robots, 2004 IEEE international conference on robotics and biomimetics, IEEE, 2004, 431-436.
- 2 M. Zhou, Y. Tian, D. Sameoto, X. Zhang, Y. Meng and S. Wen, Controllable interfacial adhesion applied to transfer light and fragile objects by using gecko inspired mushroomshaped pillar surface, ACS Appl. Mater. Interfaces, 2013, 5(20), 10137-10144.
- 3 T. Eisner and D. J. Aneshansley, Defense by foot adhesion in a beetle (Hemisphaerota cyanea), (in eng), Proc. Natl. Acad. Sci. U. S. A., 2000, 97(12), 6568-6573, DOI: 10.1073/pnas. 97.12.6568.
- 4 K. Autumn, Gecko Adhesion: Structure, Function, and Applications, MRS Bull., 2007, 32(6), 473-478, DOI: 10.1557/ mrs2007.80.
- 5 C. Creton and S. N. Gorb, Sticky feet: from animals to materials, MRS Bull., 2007, 32, 466-468.
- 6 A. Jagota and C.-Y. Hui, Adhesion, friction, and compliance of bio-mimetic and bio-inspired structured interfaces, Mater. Sci. Eng., R, 2011, 72(12), 253-292, DOI: 10.1016/ j.mser.2011.08.001.
- 7 K. Autumn, et al., Adhesive force of a single gecko foot-hair, Nature, 2000, 405(6787), 681-685.
- 8 K. Autumn and A. M. Peattie, Mechanisms of adhesion in geckos, Integrative Comparative Biol., 2002, 42(6), 1081-1090.
- 9 B. Bhushan, Bioinspired structured surfaces, Langmuir, 2012, 28(3), 1698-1714, DOI: 10.1021/la2043729.
- 10 B. Bhushan, Adhesion of multi-level hierarchical attachment systems in gecko feet, J. Adhes. Sci. Technol., 2007, 21(12-13), 1213-1258, DOI: 10.1163/156856107782328353.
- 11 M. S. Kellar Autumn, Y. A. Liang, A. M. Peattie, W. R. Hansen, S. Sponberg, T. W. Kenny, R. Fearing, J. N. Israelachvili and R. J. Full, Evidence for van der Waals adhesion in gecko setae, 2002.
- 12 H. Lee, B. P. Lee and P. B. Messersmith, A reversible wet/dry adhesive inspired by mussels and geckos, Nature, 2007, 448(7151), 338-341, DOI: 10.1038/nature05968.
- 13 S. N. Gorb, Evolution of the Dragonfly Head-Arresting System, Proc.: Biol. Sci., 1999, 266(1418), 525-535[Online]. Available: https://www.jstor.org/stable/51177.
- 14 R. G. Beutel and S. N. Gorb, Ultrastructure of attachment specializations of hexapods (Arthropoda): evolutionary patterns inferred from a revised ordinal phylogeny, J. Zoological

- Systematics Evolutionary Res., 2001, 39(4), 177-207, DOI: 10.1046/j.1439-0469.2001.00155.x.
- 15 W. Federle, E. L. Brainerd, T. A. McMahon and B. Hölldobler, Biomechanics of the movable pretarsal adhesive organ in ants and bees, Proc. Natl. Acad. Sci. U. S. A., 2001, 98(11), 6215-6220, DOI: 10.1073/pnas.111139298.
- 16 J. A. Peterson, Convergent and Alternative Designs in the Digital Adhesive Pads of Scincid Lizards, 1982.
- 17 H. A. Stone, Biological Micro- and Nanotribology: Nature's Solutions, Phys. Today, 2002, 55(6), 53, DOI: 10.1063/ 1.1496378.
- 18 A. Kesel, A. Martin and T. Seidl, Adhesion measurements on the attachment devices of the jumping spider Evarcha arcuata, J. Exp. Biol., 2003, 206(16), 2733-2738.
- 19 Z. Dai, S. N. Gorb and U. Schwarz, Roughness-dependent friction force of the tarsal claw system in the beetle Pachnoda marginata (Coleoptera, Scarabaeidae), J. Exp. Biol., 2002, 205(16), 2479-2488.
- 20 C. G. Aranzazu del Campo and E. Arzt, contact shape controls adhesion of bioinspired fibrillar structures, 2007.
- 21 S. N. Gorb, Biological attachment devices: exploring nature's diversity for biomimetics, Philos. Trans. R. Soc., A, 2008, 366(1870), 1557-1574.
- 22 D. R. King, M. D. Bartlett, C. A. Gilman, D. J. Irschick and A. J. Crosby, Creating gecko-like adhesives for "real world" surfaces, Adv. Mater., 2014, 26(25), 4345-4351.
- 23 S. N. Gorb, et al., Structural design and biomechanics of friction-based releasable attachment devices in insects, Integrative Comparative Biol., 2002, 42(6), 1127-1139.
- 24 M. Piccardo, A. Chateauminois, C. Fretigny, N. M. Pugno and M. Sitti, Contact compliance effects in the frictional response of bioinspired fibrillar adhesives, J. R. Soc., Interface, 2013, **10**(83), 20130182.
- 25 M. Scherge and S. Gorb, Biological micro-and nanotribology, Springer Science & Business Media, 2001.
- 26 M. D. Bartlett, A. B. Croll, D. R. King, B. M. Paret, D. J. Irschick and A. J. Crosby, Looking beyond fibrillar features to scale gecko-like adhesion, Adv. Mater., 2012, 24(8), 1078-1083.
- 27 H. Gao, X. Wang, H. Yao, S. Gorb and E. Arzt, Mechanics of hierarchical adhesion structures of geckos, Mech. Mater., 2005, 37(2-3), 275-285.
- 28 E. Arzt, S. Gorb and R. Spolenak, From micro to nano contacts in biological attachment devices, Proc. Natl. Acad. Sci. U. S. A., 2003, 100(19), 10603-10606, DOI: 10.1073/ pnas.1534701100.
- 29 M. G. De, US Pat., 2717437, 1955.
- 30 S. Gorb, Attachment Devices Of Insect Cuticle, 2001.
- 31 N. J. Glassmaker, A. Jagota, C.-Y. Hui, W. L. Noderer and M. K. Chaudhury, Biologically inspired crack trapping for enhanced adhesion, Proc. Natl. Acad. Sci. U. S. A., 2007, 104(26), 10786-10791.
- 32 M. Kamperman, E. Kroner, A. del Campo, R. M. McMeeking and E. Arzt, Functional adhesive surfaces with "gecko" effect: the concept of contact splitting, Adv. Eng. Mater., 2010, **12**(5), 335-348.

Paper

33 N. J. Glassmaker, T. Himeno, C. Y. Hui and J. Kim, Design of biomimetic fibrillar interfaces: 1. Making contact, *J. R. Soc. Interface*, 2004, **1**(1), 23–33, DOI: **10.1098/rsif.2004.0004**.

- 34 B. Wijerathne, T. Liao, K. Ostrikov and Z. Sun, Bioinspired Robust Mechanical Properties for Advanced Materials, *Small Struct.*, 2022, 3(9), 2100228, DOI: 10.1002/sstr.2021 00228.
- 35 R. Hensel, K. Moh and E. Arzt, Engineering micropatterned dry adhesives: from contact theory to handling applications, *Adv. Funct. Mater.*, 2018, 28(28), 1800865.
- 36 B. Bhushan, Biomimetics, *Philos Trans. A Math Phys Eng Sci*, 2009, 367(1893), 1443–1444, DOI: 10.1098/rsta.2009.0026.
- 37 M. R. Walter Federle, A. S. G. Curtis and R. J. Full, An Integrative Study of Insect Adhesion: Mechanics and Wet Adhesion of Pretarsal Pads in Ants, 2002.
- 38 S. Kim and M. Sitti, Biologically inspired polymer microfibers with spatulate tips as repeatable fibrillar adhesives, *Appl. Phys. Lett.*, 2006, **89**(26), 261911.
- 39 J. Purtov, M. Frensemeier and E. Kroner, Switchable adhesion in vacuum using bio-inspired dry adhesives, *ACS Appl. Mater. Interfaces*, 2015, 7(43), 24127–24135.
- 40 C. M. Chen, C. L. Chiang, C. L. Lai, T. Xie and S. Yang, Buckling-Based Strong Dry Adhesives Via Interlocking, (in English), *Adv. Funct. Mater.*, 2013, 23(30), 3813–3823, DOI: 10.1002/adfm.201300052.
- 41 Z. He, Z. Liu, M. Li, C. Y. Hui and A. Jagota, Meso-scale dislocations and friction of shape-complementary soft interfaces, *J. R.Soc., Interface*, 2021, **18**(175), 20200940, DOI: **10.1098/rsif.2020.0940**.
- 42 J. Dillen, Z. He, C.-Y. Hui and A. Jagota, Geometry of defects at shape-complementary soft interfaces, *Extreme Mech. Lett.*, 2016, **9**, 74–83.
- 43 A. K. Singh, Y. Bai, N. Nadermann, A. Jagota and C. Y. Hui, Adhesion of microchannel-based complementary surfaces, *Langmuir*, 2012, 28(9), 4213–4222, DOI: 10.1021/la204519w.
- 44 C. Jin, A. Jagota and C.-Y. Hui, Structure and Energetics of Dislocations at Micro-Structured Complementary Interfaces Govern Adhesion, *Adv. Funct. Mater.*, 2013, 23(27), 3453–3462, DOI: 10.1002/adfm.201203337.
- 45 S. Vajpayee, K. Khare, S. Yang, C.-Y. Hui and A. Jagota, Adhesion Selectivity Using Rippled Surfaces, Adv. Funct. Mater., 2011, 21(3), 547–555, DOI: 10.1002/adfm.201001652.
- 46 P. Guduru, Detachment of a rigid solid from an elastic wavy surface: theory, *J. Mech. Phys. Solids*, 2007, 55(3), 445–472.
- 47 P. Guduru and C. Bull, Detachment of a rigid solid from an elastic wavy surface: experiments, *J. Mech. Phys. Solids*, 2007, 55(3), 473–488.

- 48 Y. Desplanques, Amontons-Coulomb Friction Laws, A Review of the Original Manuscript, *SAE Int. J. Mater. Manuf.*, 2014, 8(1), 98–103, DOI: 10.4271/2014-01-2489.
- 49 M. Urbakh and E. Meyer, Nanotribology: the renaissance of friction, *Nat. Mater.*, 2010, 9(1), 8–10, DOI: 10.1038/nmat2599.
- 50 A. Vanossi, N. Manini, M. Urbakh, S. Zapperi and E. Tosatti, Colloquium: Modeling friction: From nanoscale to mesoscale, *Rev. Mod. Phys.*, 2013, 85(2), 529–552, DOI: 10.1103/ RevModPhys.85.529.
- 51 R. Peierls, The size of a dislocation, *Proc. Phys. Soc.*, 1940, 52(1), 34.
- 52 F. Nabarro, Fifty-year study of the Peierls-Nabarro stress, *Mater. Sci. Eng.*, *A*, 1997, **234**, 67–76.
- 53 L. Prandtl, Ein Gedankenmodell zur kinetischen Theorie der festen Körper, *ZAMM Zeitschrift für Angewandte Mathematik und Mechanik*, 1928, **8**(2), 85–106, DOI: **10.1002/zamm.19280080202**.
- 54 J. R. A. M. O. Robbins, Understanding and illustratinng the atomic origins of friction, 2004.
- 55 A. Ghatak, K. Vorvolakos, H. Q. She, D. L. Malotky and M. K. Chaudhury, Interfacial rate processes in adhesion and friction, *J. Phys. Chem. B*, 2000, 104(17), 4018–4030.
- 56 S. Sills, K. Vorvolakos, M. K. Chaudhury and R. M. Overney, Molecular origins of elastomeric friction, *Fundamentals of friction and wear*, Springer, 2007, pp. 659–676.
- 57 A. Schallamach, A theory of dynamic rubber friction, *Wear*, 1963, **6**(5), 375–382, DOI: **10.1016/0043-1648(63)90206-0**.
- 58 P. M. Anderson, J. P. Hirth and J. Lothe, *Theory of dislocations*, Cambridge University Press, 2017.
- 59 T. A. Sharp, L. Pastewka and M. O. Robbins, Elasticity limits structural superlubricity in large contacts, *Phys. Rev. B*, 2016, 93(12), 121402, DOI: 10.1103/PhysRevB.93.121402.
- 60 T. A. Sharp, L. Pastewka, V. L. Lignères and M. O. Robbins, Scale- and load-dependent friction in commensurate sphere-on-flat contacts, *Phys. Rev. B*, 2017, **96**(15), 155436, DOI: **10.1103/PhysRevB.96.155436**.
- 61 X. Xiao, J. Kaur, A. Jagota and C.-Y. Hui, Sliding friction of a pillar array interface: part II, contact mechanics of single pillar pairs, *Soft Matter*, 2024, DOI: 10.1039/d3sm01324c.
- 62 W. Bollmann, Crystal Defects and Crystalline Interfaces, Springer-Verlag, New York, 1970.
- 63 A. Merkle and L. Marks, A predictive analytical friction model from basic theories of interfaces, contacts and dislocations, *Tribol. Lett.*, 2007, **26**, 73–84.
- 64 G. O. A. Y. Nishijima, MOIRÉ PATTERNS, *Sci. Am.*, 1963, **208**(5), 54–63.